



Synchronous Rotation in the (120347) Salacia–Actaea System

Cameron Collyer^{1,2} , Estela Fernández-Valenzuela¹ , Jose Luis Ortiz³ , Bryan J. Holler⁴ , Benjamin Proudfoot¹ , Nicolás Morales³ , Rafael Morales³ , Susan Benecchi⁵ , Flavia L. Rommel¹ , Will Grundy^{6,7} , and Darin Ragozzine⁸

¹Florida Space Institute, University of Central Florida, 12354 Research Parkway, Orlando, FL 32826, USA; cpcollyerastro@gmail.com

²Department of Physics, University of Central Florida, 4111 Libra Drive, Orlando, FL 32816, USA

³Instituto de Astrofísica de Andalucía, Glorieta de la Astronomía s/n, 18008 Granada, Spain

⁴Space Telescope Science Institute, Baltimore, MD 21218, USA

⁵Planetary Science Institute, 1700 East Fort Lowell, Suite 106, Tucson, AZ 85719, USA

⁶Lowell Observatory, 1400 West Mars Hill Road, Flagstaff, AZ 86001, USA

⁷Northern Arizona University, Department of Astronomy & Planetary Science, PO Box 6010, Flagstaff, AZ 86011, USA

⁸Brigham Young University Department of Physics & Astronomy, N283 ESC, Brigham Young University, Provo, UT 84602, USA

Received 2025 June 24; revised 2025 August 26; accepted 2025 September 2; published 2025 November 24

Abstract

We report on roughly 16 yr of photometric monitoring of the trans-Neptunian binary system (120347) Salacia–Actaea, which provides significant evidence that Salacia and Actaea are tidally locked to the mutual orbital period in a fully synchronous configuration. The orbit of Actaea is updated, followed by a Lomb–Scargle periodogram analysis of the ground-based photometry, which reveals a synodic period similar to the orbital period and a peak-to-peak lightcurve amplitude of $\Delta m = 0.0900 \pm 0.0036$ mag (1σ uncertainty). Incorporating archival Hubble Space Telescope photometry that resolves each component, we argue that the periodicity in the unresolved data is driven by a longitudinally varying surface morphology on Salacia, and we derive a sidereal rotation period that is within 1σ of the mutual orbital period. A rudimentary tidal evolution model is invoked that suggests synchronization occurred within 1.1 Gyr after Actaea was captured/formed.

Unified Astronomy Thesaurus concepts: Trans-Neptunian objects (1705); Tidal friction (1698); Asteroid satellites (2207)

1. Introduction

Much of what we know about the interiors of trans-Neptunian objects (TNOs) is derived from detailed study of binary systems. Constraining the mutual orbit of a binary system (yielding a total system mass) and estimating the volume by means of stellar occultations or thermal radiometry gives a first-order estimate of its bulk composition, the mass density (density hereafter). Observations of TNOs point to a size–density relationship where density increases with size (e.g., M. E. Brown 2012; W. M. Grundy et al. 2019a). This has been interpreted as being the result of the compaction of a rock-rich core and its drop in porosity during thermal evolution and differentiation, an effect that increases with increasing size, mass, and rock mass fraction (C. J. Bierson & F. Nimmo 2019; S. Loveless et al. 2022). The spin–orbit configurations of the largest TNO–satellite systems have been reproduced by simulations of giant impacts, where the satellite is captured as an intact fragment of the impactor or forms from a collisional debris disk around the primary (e.g., S. Arakawa et al. 2019).

Here we focus on the TNO binary system (120347) Salacia–Actaea. Salacia–Actaea is dynamically classified as a hot classical main-belt TNO (B. Gladman & K. Volk 2021). The surface compositions of Salacia and Actaea are likely quite similar. Resolved Hubble Space Telescope (HST) multiband photometry shows that they have similar optical colors (S. D. Benecchi et al. 2009). The color–albedo dichotomy of TNOs (P. Lacerda et al. 2014) also suggests that the low

geometric albedo derived for the unresolved system from radiometry (E. Vilenius et al. 2012; S. Fornasier et al. 2013; M. E. Brown & B. J. Butler 2017) is representative of both surfaces. The shallow spectral slope of each component’s surface and the low geometric albedo are characteristic of the BrightIR TNO surface class (e.g., W. C. Fraser et al. 2023). The dynamically excited orbit and BrightIR surface class point to the system forming closer to the Sun and being scattered outward onto its current orbit during Neptune’s migration. The diameters of Salacia and Actaea have been measured through radiometry to be 866 ± 37 km and 290 ± 21 km, respectively (M. E. Brown & B. J. Butler 2017). Using the system mass (which we update in this work; see Section 2) and total system volume, the effective density of the system is $\rho = 1.38^{+0.22}_{-0.18}$ g cm^{−3}. This density appears to be intermediate between low-mass, highly porous worlds and the dwarf planet class, where significant central compaction is expected. Other TNO worlds in this intermediate size–density regime are (90482) Orcus, (38628) Huya, (174567) Varda, (55637) 2002 UX25, and (229762) G!kún||’hòmdímà.

In this work, we present observational evidence that supports the Salacia–Actaea system being fully tidally evolved today, where lightcurve analysis points to Salacia rotating at the mutual orbital period. We utilize the tidal evolution model of P. Goldreich & S. Soter (1966), which predicts total synchronization of Salacia–Actaea within the age of the solar system if Salacia’s interior is within an order of magnitude as dissipative as the interior of (136199) Eris. In light of these results, we propose other TNO systems that may also be synchronized and suggest future work that could further constrain the properties of TNO interiors in the intermediate-density regime.



Original content from this work may be used under the terms of the [Creative Commons Attribution 4.0 licence](https://creativecommons.org/licenses/by/4.0/). Any further distribution of this work must maintain attribution to the author(s) and the title of the work, journal citation and DOI.

2. The Mutual Orbit

In this section, we update the orbit for the Salacia–Actaea system, which was last updated based on observations in 2016 (W. M. Grundy et al. 2019b). To do this, we acquired three new resolved observations of Salacia and Actaea, one with Keck in 2021 and two with HST in 2024, increasing the observational baseline by 8 yr. Our full astrometry dataset is described in Appendix A. Orbit fitting was completed using MultiMoon, an orbit fitter built for TNO binary orbit fitting (B. C. Proudfoot et al. 2024; D. Ragozzine et al. 2024). The dataset we used was taken verbatim from W. M. Grundy et al. (2019b), although with our added observations. See Appendix A for further details regarding these observations and the orbit fitting procedure. Our derived orbit is nearly identical to the most recent found in the literature (W. M. Grundy et al. 2019b), although the recovered parameters are somewhat more precise (see Table 1 for the full Keplerian orbit solution).

Two results of particular relevance here are the updated system mass and mutual orbital period, being $M_{\text{sys}} = 486.1^{+7.6}_{-7.4} \times 10^{18}$ kg and $P_{\text{orb}} = 5.49389 \pm 0.00001$ days, respectively. Using the diameters of Salacia and Actaea derived in M. E. Brown & B. J. Butler (2017; 866 ± 37 km and 290 ± 21 km, respectively) to calculate the total system volume, this yields an effective bulk density of $\rho = 1.38^{+0.22}_{-0.18}$ g cm $^{-3}$ for the system. This density is roughly 10% larger than the bulk density derived in M. E. Brown & B. J. Butler (2017) due to the larger updated system mass.

3. Lightcurve Observations and Photometry

3.1. Description of Observations

The ground-based photometry used in this work was obtained from 2005 August to 2021 October. The total on-target time was ~ 165 hr, or ~ 6.90 days. Roughly 20% of the observations were made before 2010, 60% between 2011 and 2015, and 20% after 2020 January. Observations were made with 11 different telescope/camera/filter combinations. A description of the hardware used along with the number of observing runs and images for each telescope/camera/filter combination is tabulated in Table 2.

3.2. Absolute Magnitude Calibration

We utilized the Massive prOcessing Of aStronomical imagEs (Moose) version 2 (M2; R. Morales et al. 2022) software to process FITS images from each observing run and output photometry of the Salacia–Actaea system. Photometry is calibrated to the Johnson–Cousins R band on the A. U. Landolt (1992) photometric system. In Appendix B, we describe the M2 software and the method used to transform the photometry.

The heliocentric and geocentric distances and Sun–TNO–Earth phase angle⁹ varied over the course of the ~ 16 yr of observations. This would obscure any photometric periodicity we look to measure from the system, and so we needed to transform to a constant geometry. The absolute magnitude H of a small body is the magnitude it would have if it were located at the (impossible) geometry $\Delta = r = 1$ au and a phase angle of $\alpha = 0^\circ$, where Δ is the geocentric distance and r is the

Table 1
Keplerian Orbit Solution for Salacia–Actaea

Parameter	Symbol	Posterior
Fitted Parameters		
System mass (10^{18} kg)	M_{sys}	$486.1^{+7.6}_{-7.4}$
Semimajor axis (km)	a	5700^{+30}_{-29}
Eccentricity	e	$0.008^{+0.003}_{-0.003}$
Inclination (deg)	i	$17.2^{+0.5}_{-0.5}$
Argument of periaapsis (deg)	ω	41^{+33}_{-22}
Longitude of the ascending node (deg)	Ω	$108.9^{+1.6}_{-1.6}$
Mean anomaly at epoch (deg)	\mathcal{M}	157^{+27}_{-22}
Derived Parameters		
Orbit period (days)	P_{orb}	$5.49389^{+0.00001}_{-0.00001}$
Orbit pole R.A. (deg)	α_{orb}	$313.7^{+1.2}_{-1.2}$
Orbit pole decl. (deg)	δ_{orb}	$66.1^{+0.5}_{-0.5}$
Orbit pole lon. (deg)	λ_{orb}	$18.9^{+1.6}_{-1.6}$
Orbit pole lat. (deg)	β_{orb}	$72.8^{+0.5}_{-0.5}$

heliocentric distance. In order to remove the phase-angle dependence on the photometry, we constrained the phase curve of the Salacia–Actaea system for phase angles α in the range $0.5 \lesssim \alpha \lesssim 1.3$. Over this range of phase angles, we noted that the phase curve of the Salacia–Actaea system is virtually consistent with a linear trend, so we chose a simple linear model for the phase curve. When the phase function contribution is approximated as linear, the H -magnitude equation is

$$H = m - 5 \log(r\Delta) - \beta\alpha, \quad (1)$$

where β is the linear phase coefficient with units of mag deg $^{-1}$, m is the apparent magnitude (R band), and Δ and r are in units of au. We highlight that the H_R reported here for Salacia–Actaea is calculated without constraints on the phase function at the lowest phase angles, where we may be missing a nonlinear opposition surge (e.g., A. J. Verbiscer et al. 2022). This H_R magnitude may therefore be an overestimate of the true H_R , and so we refer to it as $H_{R,\beta}$. Though this may be true, it has no effect on our period search since it removes all relative phase-angle dependence. We find $H_{R,\beta}$ and β to be 3.8094 ± 0.0049 mag and 0.1284 ± 0.0048 mag deg $^{-1}$, respectively, as shown in Figure 1.¹⁰

If the photometric phase is parameterized by the variable θ , where $\theta \in [0, 1]$, we define the H magnitude as the period average of

$$h(\theta) = H + f(\theta), \quad (2)$$

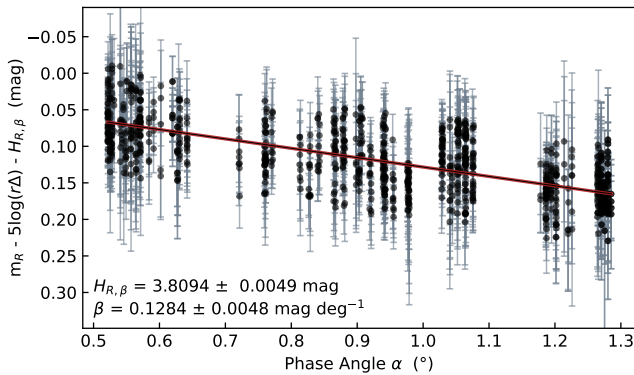
where $f(\theta)$ represents the period phase dependence with a period average of 0. In analyzing the absolute magnitude of the system over ~ 16 yr of observations, we find no evidence of a systematic change in $H_{R,\beta}$.

⁹ Heliocentric and geocentric distances and Sun–Earth–TNO phase angles were queried from the JPL SBDB (https://ssd.jpl.nasa.gov/tools/sbdb_lookup.html#/?sstr=salacia) using Astroquery (A. Ginsburg et al. 2019).

¹⁰ The phase curve, $H_{R,\beta}$, and β fit parameters explicitly presented here were evaluated after the analysis in the following section. The photometric periodicity was removed. See Appendix B, which explains this iterative procedure.

Table 2
Observation Description

Telescope Name	Diameter (m)	CCD Camera	Bin	$x \times y$ (pixels \times pixels)	s (arcsec pixel $^{-1}$)	FOV	Filter	N_O^a	N_m^b	Date Span
CAHA ^c	1.2	DLR-MKIII	2×2	2048×2056	0.63	$21'4 \times 21'4$	<i>O</i>	8	148	2014.96–2021.78
CAHA ^c	2.2	SITe-1d	2×2	1024×1024	0.53	$9' \times 9'$	<i>R</i>	6	10	2011.73–2012.79
	<i>V</i>	6	8	2011.73–2012.79
	<i>KG</i>	7	27	2011.66–2011.83
CAHA ^c	3.5	SITe-16a	2×2	1000×1000	0.64	$11' \times 11'$	<i>R</i>	1	1	2014.55–2014.55
	<i>V</i>	1	2	2014.55–2014.55
NOT ^d	2.6	ALFOSC	1×1	2048×2064	0.21	$6'4 \times 6'4$	<i>R_B</i>	1	4	2011.66–2011.66
OSN ^e	1.5	Roper T150	2×2	1024×1024	0.46	$7'9 \times 7'9$	<i>O</i>	45	572	2005.59–2021.76
TNG ^f	3.6	DOLORES	2×2	1050×1050	0.51	$8'6 \times 8'6$	<i>I</i>	2	8	2011.50–2011.51
	<i>R</i>	10	194	2011.50–2011.83
	<i>V</i>	4	14	2011.50–2011.51

Notes.^a Number of individual observing runs.^b Cumulative number of photometric data points from all observing runs.^c Calar Alto Astronomical Observatory, Spain.^d Nordic Optical Telescope, Canary Islands.^e Sierra Nevada Observatory, Spain.^f Galileo National Telescope, Canary Islands.**Figure 1.** The magnitude dependence as a function of the Sun–TNO–Earth phase angle α . Over the $0.5^\circ \lesssim \alpha \lesssim 1.3^\circ$ range, the relationship is clearly linear.**4. Period Search**

We conducted a period search on the photometric data (h mags) using Astropy’s Time Series LombScargle class (Astropy Collaboration et al. 2013, 2018, 2022), which invokes the Lomb–Scargle (N. R. Lomb 1976; J. D. Scargle 1982) periodogram (periodogram hereafter) on time-series data and takes uncertainties into account. We searched for sinusoidal signals in the periodogram analysis; a peak in the periodogram at frequency f_i suggests that there is a photometric signal from the data of the form $h_R = H_R + A \cos(2\pi f_i t + \phi)$. The following periodogram analysis follows the guiding work of J. T. VanderPlas (2018).

4.1. Periodogram of the Window Function

We first analyzed a periodogram of the time sampling (window function) to constrain how the observation windowing distorts the periodogram of the photometry. Any unique frequencies with nonzero powers in the window periodogram (1) may show up as false peaks in the periodogram of the photometry and (2) create aliases of the true photometric

frequencies exhibited by the Salacia–Actaea system. If Salacia–Actaea exhibits a real photometric frequency at f_{real} , then each window frequency f_w produces aliases of f_{real} along the sequences

$$\begin{aligned} f_{\text{real}} \pm k f_w, \\ -f_{\text{real}} \pm k f_w, \quad k = 1, 2, 3, \dots, \pm\infty. \end{aligned} \quad (3)$$

When assessing the periodogram of the photometry itself, peaks in the power spectrum corresponding to frequencies along these sequences are therefore derived from the true driving frequency f_{real} and are not unique (J. T. VanderPlas 2018).

We created the window function by setting all values of the photometry to unity. In evaluating the window periodogram, we did not precenter the data or use a floating mean. The periodogram of the window function revealed that the main frequencies arising from the time sampling were (1) Earth’s sidereal rotation period (~ 0.9972 day) and (2) the synodic period of the Moon (~ 29.527 days).

4.2. Periodogram of the Salacia–Actaea Photometry

We now present the results of the periodogram analysis of the unresolved ground-based photometry of the Salacia–Actaea system. An initial power spectrum using a frequency grid with an upper bound of 1 cycle hr^{-1} showed that frequencies above 2.5 cycles day^{-1} corresponded to very small normalized powers, and so we focused on frequencies lower than 2.5 cycles day^{-1} , corresponding to periods greater than 9.6 hr. The 6.5 hr photometric period of the system published in A. Thirouin et al. (2014, hereafter T14) did not appear to be a driving frequency in our periodogram analysis, though it is close to the $k = 4$ alias of the main frequency found below (see also Section 4.4).

In order to evaluate the noise floor of the spectral power in the periodograms, we bootstrap-resampled the photometry by randomly reassigning h mags and their uncertainties to the timing array. We did this 10,000 times. For each bootstrap run, the maximum power achieved was recorded. In Figure 2 (left), the power corresponding to the height of the gray box is the

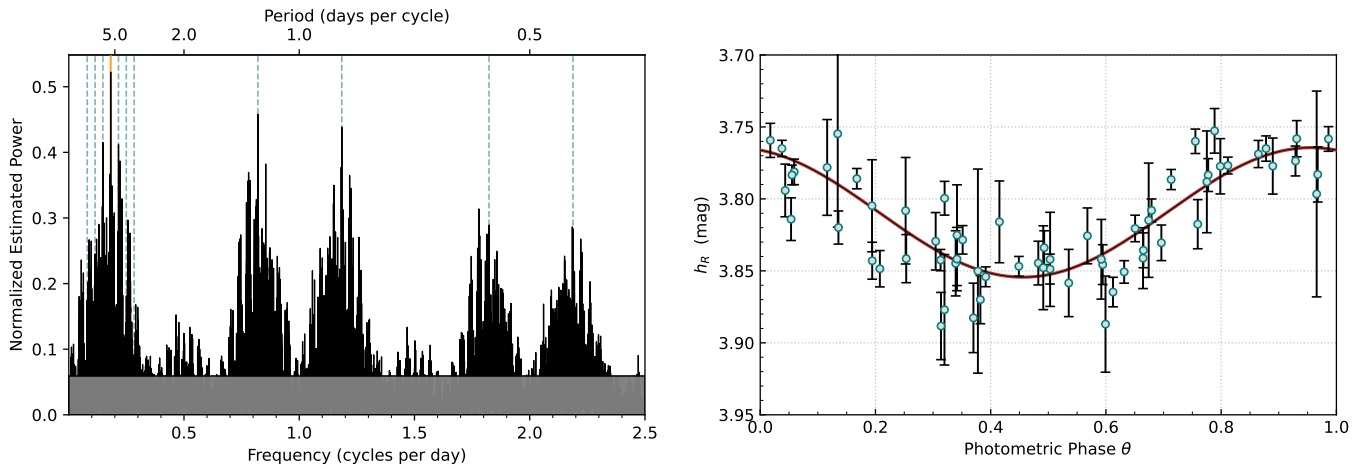


Figure 2. Left: Lomb-Scargle periodogram of the unresolved ground-based photometry of the Salacia-Actaea system in the range where spectral powers are significant. The frequency with the highest power, ~ 0.182 cycles day^{-1} , is highlighted in orange. The blue dashed lines are the expected locations of aliases of this frequency (up to $k = 3$) due to the windowing frequencies (see Section 4.1). Right: the time-series photometry (h mags vs. time) folded over the synodic period $T_{\text{syn}} = 5.49430$ days. Since this period is much larger than the time span of any single observing run when photometry was measured, we plot the weighted average of each observing run and its uncertainty. The fact that multiple observing runs that sample the same rotational phase are in agreement bolsters confidence that this period is legitimate. The solid red line is the best-fit phase-shifted sinusoid.

largest normalized estimated power achieved in the bootstrapping runs, where peaks above this noise floor have a 0.1% false-positive rate (J. T. VanderPlas 2018). Spectral powers above this line, generally speaking, are therefore caused by true photometric periodicities and their aliases with 99.9% confidence.

The frequency corresponding to the highest power in the periodogram was ~ 0.182 cycles day^{-1} , with an equivalent period of ~ 5.494 days. This is similar to Actaea’s orbital period of 5.49389 ± 0.00001 days (Table 1). We performed 10,000 Monte Carlo runs of the periodogram by resampling each photometric data point from a Gaussian centered at the measured h -mag mag and scaled by its uncertainty. In all 10,000 runs, the same frequency of 0.182 cycles day^{-1} showed the highest spectral power. The structures seen in this periodogram correspond to aliases of the 0.182 cycles day^{-1} frequency and aliases of those aliases.

4.3. Phase-folded Lightcurve

In Figure 2 (right), we folded the time-series photometry by the ~ 5.494 day period, which revealed an underlying signal with a sinusoidal shape. Since this period is much longer than the time span of any single observing run when photometry was measured, we plot the weighted average of each observing run and its uncertainty. Note that the periodogram analysis of the previous section was done on the nonbinned photometry.

The best-fit synodic photometric period T_{syn} and peak-to-peak amplitude Δm with their corresponding 1σ uncertainties are $T_{\text{syn}} = 5.49430 \pm 0.00016$ days and $\Delta m = 0.0900 \pm 0.0036$ mag. Gaussian uncertainties for the period as well as for the amplitude of the lightcurve were determined as follows, using the period as an example. We used a hyperfine grid of trial periods (finer than the periodogram grid spacing) around the best-fit period and stepped through each period, phase folding the data by this period and fitting a phase-shifted cosine function, allowing the amplitude to be a free parameter. The uncertainty in the period corresponds to the difference between the best-fit period and the period where the minimum

χ^2 increased by unity. The same was done for an amplitude grid centered on the best-fit amplitude. We find the uncertainties on each parameter to be symmetric. In the following sections, we discuss the nature of this periodicity.

4.4. Considering Previous Results for Rotation

As noted above, the photometric periodicity of $T_{\text{syn}} = 5.49430 \pm 0.00016$ days is discrepant with the results of T14, who found $T_{\text{syn}} \simeq 6.5$ hr. We would like to highlight that the ground-based photometry dataset used in the present work is $4\times$ as large as the dataset published in T14. Moreover, we computed absolute photometry on the images used in T14 and incorporated this into our dataset. The relative photometry used in T14 to search for periodicity in the Salacia-Actaea system is biased toward detecting short-period signals less than the duration of their observing runs (1–4 days). In comparison, the absolute photometry and larger dataset used in the present work is more sensitive to longer-period fluctuations and allows multiyear observations to be combined with greater accuracy in the zero-point of the photometry.

We also downloaded the photometry from T14 and ran a periodogram analysis. To reproduce the results of T14, we needed to remove the uncertainties when generating the periodogram; when uncertainties were included, we found that the 5.49430 day period had the highest estimated power in the spectrum. The relative photometry was phase folded by periods of 5.49430 days and 6.5 hr, and we calculated the χ^2 per degree of freedom for each case, yielding values of 1.17 and 1.42, respectively. The smaller reduced χ^2 for the 5.49430 day period is consistent with the results from the periodogram utilizing the uncertainties, as well as the results from Section 4.2. The 6.5 hr period is also close to the $k = 4$ alias of 5.49430 days. We conclude that the 6.5 hr period found in T14 is the result of their photometry technique being biased toward detecting short-period signals, and that they likely detected a short-period alias of the true 5.49430 day synodic period.

5. Synchronous Rotation

5.1. Resolved HST Observations

In order to understand the nature of the photometric signal that appears to oscillate with the same period of Actaea’s orbit, we analyzed archival HST data of the system that resolved Salacia and Actaea individually. We analyzed HST images obtained with the Planetary Camera (PC) of the Wide Field and Planetary Camera 2 (WFPC2; M. McMaster et al. 2008) that were part of HST Cycle 16 program 11178 (PI: Will Grundy).¹¹ The dates of these images span 2007 July 15–2008 May 19. Resolved point-spread function (PSF) photometry was performed on data taken in the F606W filter following the method described in S. D. Benecchi et al. (2009). Collectively, there are $n = 6$ photometric points that sample Salacia’s and Actaea’s individual lightcurves. Each point represents the weighted average and the standard deviation on the mean of photometry done on individual frames; there were four dither positions for each visit, although one point is comprised of five individual frames taken over two consecutive HST orbits for which F606W – F814W color data were measured. F606W magnitudes were converted to R -band magnitudes by combining the resolved HST photometry and fitting an F606W – R color offset between the HST data (F606W band) and the model fitted to the unresolved data (R band) (Figures 2 and 3). We assume this color for Salacia and Actaea, which is a safe assumption given their almost identical F606W – F814W colors (S. D. Benecchi et al. 2009). Their apparent magnitudes were converted to h_R magnitudes using the phase curve from Section 3.2.

In Figure 3, the resolved HST data converted to h_R magnitudes are presented in the lower two panels. The epoch of these HST observations was within the time span of the ground-based observations, and so we folded the time-series data by T_{syn} . The period phase uncertainty for each data point is smaller than the width of the symbols. In the top panel, we combined the resolved HST photometry and plotted this over the ground-based photometry, which shows a close agreement.

At the outset, we highlight that a photometric periodicity consistent with the mutual orbit period observed in the periodogram analysis is unlikely to be caused by either Salacia or Actaea being triaxial ellipsoids. The lightcurve shape of a triaxial ellipsoid over a full rotation period is “double-peaked,” meaning there are two minima and two maxima per full rotation. Taking photometry of such a triaxial ellipsoid and performing a period search as described in Section 4, the periodogram would show a peak at a frequency equivalent to half of the full rotation period as it searches for sinusoidal signals. If we consider that the observed photometric periodicity of the system is due to an elongated shape, then the true rotation period of the body would be twice the mutual orbit period, such that it would be in the 1:2 spin–orbit resonance. As described in Section 6, it is likely that the Salacia–Actaea system has widened over time due to tidal evolution, where Salacia was spun down while the semimajor axis increased. If Salacia or Actaea is in the 1:2 spin–orbit resonance, it would have had to pass the 1:1 spin–orbit resonance (assuming the initial spin period was faster than

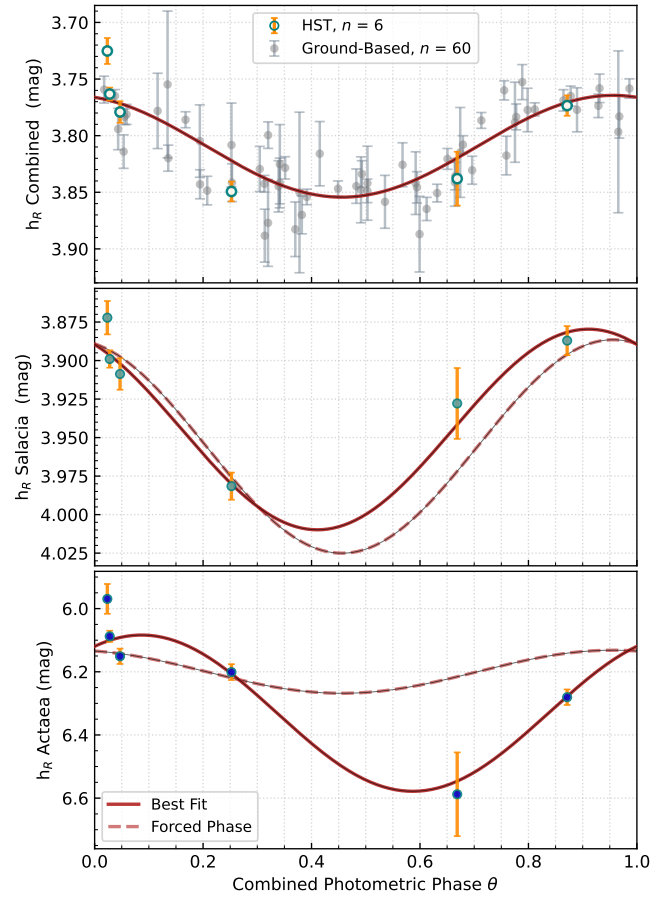


Figure 3. Top: in gray are the ground-based data from Figure 2. Data in orange/blue are the combined HST data of the system that clearly match the ground-based data. The solid line model is the best-fit phase-shifted sinusoid. Middle: resolved HST photometry of Salacia. The dashed line is a sinusoid fit to the data, where the phase offset was set to match that of the unresolved data in the top panel. The solid line is another phase-shifted sinusoid with all free parameters. Bottom: resolved HST photometry of Actaea. The styles of the lines match the model types applied to the Salacia data.

~5.494 days), which is unlikely. Therefore, the lightcurve amplitude is most likely due to a nonuniform albedo on the surface of Salacia and/or Actaea, which we discuss below.

Since Actaea is much smaller and much less massive than Salacia, Actaea’s synchronization timescale (the time it takes for Actaea’s primordial rotation period to synchronize with the orbital period) is shorter than that of Salacia. It is expected that Actaea’s orbit and spin period are synchronized today (see Section 6). We therefore first tested the hypothesis that only Actaea exhibits synchronous rotation and drives the periodicity seen in the ground-based data. Under this hypothesis, Actaea’s lightcurve shape is single-peaked, and the observed photometric periodicity is due to a nonuniform surface morphology over the longitudinal zones such as a nonuniform albedo. We first assume that Salacia’s lightcurve is constant at the weighted average of its resolved HST photometry and that Actaea’s mean flux contribution is well approximated by the weighted average of its resolved HST photometry. Under these assumptions, Actaea’s lightcurve amplitude must be $\Delta m \simeq 0.95$ mag for the combined photometry to exhibit $\Delta m \simeq 0.09$ mag (Figure 2). This lightcurve amplitude translates to a large albedo dichotomy across Actaea’s surface. Due to the nonequatorial aspect at which we view Actaea, assuming that Actaea’s spin pole is closely aligned with the

¹¹ The HST data presented in this article were obtained from the Mikulski Archive for Space Telescopes (MAST) at the Space Telescope Science Institute. The specific observations analyzed can be accessed via doi:10.17909/0ky9-sp71.

orbit pole direction, a substantial portion of Actaea’s surface near the pole is always visible. This increases the longitudinal albedo contrast required to match the lightcurve amplitude. If we assume that Actaea’s minimum albedo is the low system albedo derived from unresolved radiometry, $p_{\min} \simeq 0.04$, $p_{\max} \simeq 0.14$ yields $\Delta m \simeq 0.95$ mag. While these individual albedos are not extreme for TNOs, such a dichotomy across a small-sized TNO like Actaea is difficult to reconcile even with a curated collisional story.

Moreover, if Actaea is responsible for the observed photometric periodicity, then its period-folded HST photometry must oscillate in phase with the unresolved photometry. We fitted a simple sinusoidal model to the Actaea photometry by forcing it to be in phase with the ground-based photometry. This resulted in a poor fit with $\Delta m \simeq 0.18$ mag, significantly smaller than the $\Delta m \simeq 0.95$ mag required to match the observations (dashed line in bottom panel of Figure 3). Salacia’s lightcurve is also clearly not constant as assumed, which in turn would require $\Delta m > 0.95$ for Actaea’s lightcurve to wash out Salacia’s oscillating signal. Collectively, these arguments do not support the hypothesis that the photometric periodicity observed in the ground-based data is due to Actaea alone.

We then turn to the hypothesis that Salacia and Actaea are doubly synchronous,¹² where Salacia’s lightcurve is single-peaked and drives the photometric periodicity observed in the ground-based data. We followed the same methodology described above. A simple sinusoidal model fitted to Salacia’s HST photometry (solid line in the middle panel of Figure 3) resulted in a good fit that is nearly in phase with the ground-based signal and $\Delta m \simeq 0.1$ mag. Assuming that Salacia’s surface has a hemispheric albedo dichotomy, this yields an albedo difference of $\sim 5\%$; concentrating an “albedo spot” to a smaller area results in a larger contrast. A similar model forcing the phase offset to be equal to that of the ground-based data resulted in an adequate fit (dashed line). The simplest explanation for the photometric periodicity found in the unresolved data is therefore that Salacia’s longitudinal zones are moderately nonuniform in albedo. The true lightcurve shapes of Salacia and Actaea are more complex than the simple sinusoid models presented here. However, use of a more complicated model is unjustified with only $n = 6$ data points. Nevertheless, the combined lightcurve shape is clearly well approximated by this simple model. These results support the hypothesis that Salacia and Actaea exhibit doubly synchronous rotation.

5.2. The Sidereal Rotation Period

The synodic photometric period found in the unresolved ground-based photometry therefore corresponds to the mutual synodic rotation period of Salacia and Actaea ($T_{\text{syn}} = 5.49430 \pm 0.00016$ days). The orbital period of Actaea, 5.49389 ± 0.00001 days (Table 1), is a sidereal period. The sidereal rotation period T_{sid} can be estimated from $T_{\text{sid}}^{-1} = T_{\text{syn}}^{-1} + \frac{\omega_{\text{sys}}}{2\pi}$, where ω_{sys} is the representative heliocentric orbital angular velocity of the system during the observations (~ 0.000569 rad day⁻¹). We find the sidereal rotation period to be $T_{\text{sid}} = 5.49403 \pm 0.00016$ days, which is consistent with Actaea’s sidereal orbital period within 1σ . This is only the

third TNO binary system observationally confirmed to exhibit doubly synchronous rotation; the Pluto–Charon (J. W. Christy & R. S. Harrington 1978) and Eris–Dysnomia (G. M. Bernstein et al. 2023; R. Szakáts et al. 2023) systems are also in this tidal end state.

6. Tidal Evolution

Doubly synchronous rotation is the end state of tidal evolution, where angular momentum transfer between rotation and orbit ceases. The present-day rotation period of ~ 5.49 days is very slow compared to typical rotation periods of singleton TNOs (~ 10 hr; e.g., M. Alexandersen et al. 2019; E. Ashton et al. 2023). It is therefore likely that the orbital separation between the two components was smaller in the past and expanded to its current value (~ 13.2 Salacia radii, R_p) through the transfer of angular momentum from Salacia’s spin to the orbit. In Appendix C, we present equations that govern the evolution of Salacia’s spin period and the orbital separation of the system (the orbital period). The purpose of this section is to explore the range of initial conditions (primaricentric semimajor axes a_0 and Salacia spin periods T_{p0}), mass ratios q , and tidal parameters that allow the system to synchronize within the age of the solar system. In the following, we assume that Actaea’s spin is always synchronized to the orbit, as its spin angular momentum is negligible compared to the spin angular momentum of Salacia and the orbital angular momentum.

The mass ratio q ($q = m_s/M_p$) for Salacia–Actaea is unknown. Conserving the system mass ($M_{\text{sys}} = 486.1^{+7.6}_{-7.4} \times 10^{18}$ kg; Table 1), we allowed the density of Actaea to range from 0.5 g cm^{-3} to the effective system density of $\rho = 1.38^{+0.22}_{-0.18} \text{ g cm}^{-3}$, corresponding to $0.013 \lesssim q \lesssim 0.037$; $\rho = 0.5 \text{ g cm}^{-3}$ is representative of comet nuclei, while the size–density relationship for TNOs (density increases with size) suggests that Actaea is less dense than Salacia. In order for outward migration to occur, the initial rotation period of Salacia T_{p0} must be shorter than the initial orbital period T_{n0} . For a test initial semimajor axis a_0 , T_{p0} is constrained by conservation of angular momentum. If $T_{p0} > T_{n0}$, outward migration is nonviable. In Figure 4(a), we show the a_0 – q parameter space where outward migration is viable by this simple argument. Our testing showed that the tidal locking time t_{lock} , the time it takes for Salacia to be spun down to the orbit period, is a strong function of q and virtually independent of a_0 . S. Arakawa et al. (2021) found that impact-forming satellites usually circularize within the range $3R_p \leq a_0 \leq 8R_p$, so Figure 4(a) plots this range.

In Figure 4(b), we show the tidal locking time t_{lock} as a function of the mass ratio q and dissipation factor Q (see Appendix C). We used $a_0 = 9R_p$, where all q values allow outward migration. In the range $50 \leq Q \leq 1250$, $t_{\text{lock}} < 1$ Gyr for $0.013 \lesssim q \lesssim 0.037$. We note that t_{lock} approaches the age of the solar system as Q approaches 10,000.

Further insight into the dynamical history of Salacia and Actaea can be understood by using the (136199) Eris–Dysnomia system as an analog. Previous work suggests that the Eris–Dysnomia system also exhibits doubly synchronous rotation (G. M. Bernstein et al. 2023; R. Szakáts et al. 2023). Working with this assumption, we show the same plots for the Eris–Dysnomia system in Figure 4 (bottom row). Conserving the system mass ($M_{\text{sys}} = 16,466 \pm 85 \times 10^{18}$ kg), we allowed the density of Dysnomia to range from 0.5 g cm^{-3} to the effective system density of $\rho = 2.43 \pm 0.05 \text{ g cm}^{-3}$, corresponding to $0.0055 \lesssim q \lesssim 0.027$ (B. J. Holler et al.

¹² Since Actaea’s synchronization timescale is much shorter than Salacia’s, it follows that if Salacia’s rotation is synchronized, Actaea’s is as well.

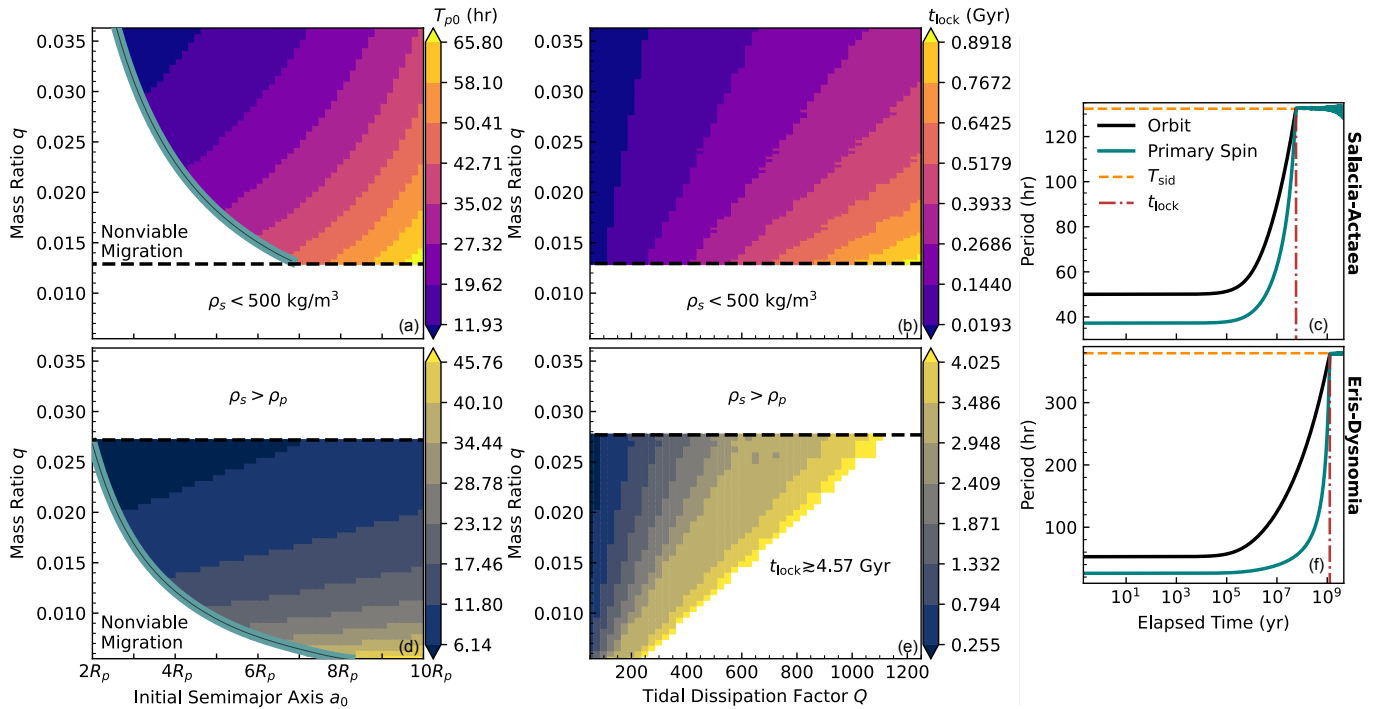


Figure 4. The top row is for the Salacia–Actaea system. (a) a_0 – q – T_{p0} space, where outward migration is viable by conservation of angular momentum. The range of q values is calculated by allowing Actaea’s density to range from 0.5 g cm^{-3} up to the effective system density of $\rho = 1.38^{+0.22}_{-0.18} \text{ g cm}^{-3}$. (b) Three-dimensional plot that shows the dependence of the tidal locking time t_{lock} on Q and q . (c) A schematic example of an integration where Actaea migrates outward while spinning down Salacia. In this example, tidal evolution ceases at $t_{\text{lock}} \simeq 50 \text{ Myr}$. The bottom panels are the same figures but represent the Eris/Dysnomia system.

2021). Using the same range of dissipation factors Q , the tidal locking time t_{lock} for Eris–Dysnomia is approximately an order of magnitude longer than that of Salacia–Actaea. In order for Eris–Dysnomia to synchronize within the age of the solar system, this places an upper limit on Q for a given q (the tidal locking timescale $\tau \propto q^{-1}$, and $\tau \propto Q$). Allowing Eris and Dysnomia to have the same density ($q \simeq 0.027$), Q can be as large as $Q_{\text{Eris}} = 1175$. The 3σ upper limit to the Dysnomia/Eris mass ratio is $q = 0.015$ (M. E. Brown & B. J. Butler 2023). From Figure 4(e), this places an upper limit on Q , such that $Q_{\text{Eris}} < 650$. For Salacia–Actaea, $Q_{\text{Salacia}} = 650$ corresponds to a tidal locking time range of $150 \text{ Myr} < t_{\text{lock}} < 400 \text{ Myr}$. If Salacia’s interior is as dissipative as that of Eris, Salacia’s spin period became locked to the orbital period within 400 Myr after Actaea was captured/formed. Even if Salacia is half as dissipative as Eris ($Q_{\text{Salacia}} = 1300$), $t_{\text{lock}} < 1.1 \text{ Gyr}$.

We note that the tidal model utilized in this work to examine the rotation period evolution is simplistic; it assumes a homogeneous rock–ice composition and does not model the temporal evolution of the interior of the primary. F. Nimmo & M. E. Brown (2023) evolved the Eris–Dysnomia system using a differentiated three-layer model of Eris consisting of a purely elastic 30 km thick ice lithosphere on top of an isoviscous 90 km thick ice shell over a rigid silicate core. In that work, they set the tidal dissipation factor, Q , to be a function of the time-varying internal temperature of Eris as well as the evolving forcing period ($P_{\text{force}} = 2\pi/[\Omega(t) - n(t)]$; see Appendix C), where Q is inversely proportional to temperature and P_{force} . Since Eris cooled down over time, while the forcing period increased, they found that these two time-dependent effects on Q roughly canceled each other out such that Q was virtually constant with time at $Q \simeq 420$ when using a mass

ratio $q = 0.0084$. For the constant- Q model used in the present work, and using the same mass ratio, Figure 4 requires $Q_{\text{Eris}} \lesssim 400$ for the system to synchronize within the age of the solar system. We conclude that our simple tidal evolution model is adequate for estimating tidal locking timescales.

7. Discussion

Under the assumption that Salacia’s dissipation factor, Q_{Salacia} , is approximately within an order of magnitude of that of Eris ($Q_{\text{Eris}} < 650$), our rudimentary tidal evolution model predicted that Salacia and Actaea would tidally lock in a doubly synchronous state within the age of the solar system. If we let $Q_{\text{Salacia}} = Q_{\text{Eris}}$, the Salacia–Actaea tidal locking time t_{lock} falls in the range $150 \text{ Myr} < t_{\text{lock}} < 400 \text{ Myr}$. Observations of the Salacia–Actaea system presented in this work support the hypothesis that they exhibit doubly synchronous rotation.

In light of these observations, where long time baseline photometry revealed a longer photometric period than much shorter baseline photometry, other TNO binary systems may be much more tidally evolved than short time baseline photometry has indicated. We applied the same tidal evolution model and methodology to the (90482) Orcus–Vanth system, where recent lightcurve analysis of this TNO system suggested nonsynchronous rotation (C. Kiss et al. 2020). Constraining the rotation period of Orcus by lightcurve analysis is challenging due to the small aspect angle at which we view the system. Assuming that the spin pole of Orcus is within a few degrees of the mutual orbit pole, the average aspect angle over the past $\sim 20 \text{ yr}$ has been $\psi \simeq 27^\circ$. This can be compared to the larger $\psi \simeq 51^\circ$ aspect angle at which we observe Salacia–Actaea. The mass ratio of the Orcus–Vanth system has been constrained by M. E. Brown & B. J. Butler (2023). Assuming the 3σ lower limit to the mass ratio ($q = 0.12$), the

spin periods of Orcus and Vanth synchronized within the age of the solar system even when we allowed the tidal dissipation factor to be an order of magnitude greater than the upper limit derived for Eris ($Q_{\text{Eris}} < 650$; recall $\tau \propto q^{-1}$, and $\tau \propto Q$); Orcus and Vanth have likely tidally evolved to become fully synchronized as initially suggested in M. E. Brown & B. J. Butler (2023).

We encourage future observations to test the hypothesis that the TNO systems Orcus–Vanth and (174567) Varda–Ilmare, as well as (38628) Huya and its satellite, are doubly synchronous. The (229762) G!kún||'hòmdímà–G!ò'é !Hú system is of particular interest; the likely low mass fraction $q \simeq 0.011$ and large semimajor axis $a \simeq 19R_p$ (W. M. Grundy et al. 2019a) suggest that the synchronization timescale is approximately an order of magnitude longer than that of the Salacia–Actaea system, similar to the Eris–Dysnomia system. If this system is indeed synchronized, this would point to G!kún||'hòmdímà's interior being quite dissipative and would call for more complex thermal-orbit modeling (e.g., F. Nimmo & M. E. Brown 2023; R. Akiba & F. Nimmo 2025).

Under the previously held inference that the Salacia–Actaea and Orcus–Vanth systems are not synchronized, as evidenced by past short time baseline lightcurve analysis, S. Arakawa et al. (2025) showed that this was consistent with Orcus and Salacia having low rock mass fractions, similar to comets. Our finding that Salacia and Actaea are fully synchronized calls for future investigations into the rock mass fractions present in Salacia, Orcus, and other TNOs.

Acknowledgments

This research is based on observations made with the NASA/ESA Hubble Space Telescope obtained from the Space Telescope Science Institute, which is operated by the Association of Universities for Research in Astronomy, Inc., under NASA contract NAS 5–26555. These observations are associated with program 17848.

Some of the data presented herein were obtained at Keck Observatory, which is a private 501(c)3 nonprofit organization operated as a scientific partnership among the California Institute of Technology, the University of California, and the National Aeronautics and Space Administration. The Observatory was made possible by the generous financial support of the W. M. Keck Foundation.

This work has made use of data from the European Space Agency (ESA) mission Gaia (<https://www.cosmos.esa.int/gaia>), processed by the Gaia Data Processing and Analysis Consortium (DPAC; <https://www.cosmos.esa.int/web/gaia/dpac/consortium>). Funding for the DPAC has been provided by national institutions, in particular the institutions participating in the Gaia Multilateral Agreement.

The authors wish to recognize and acknowledge the very significant cultural role and reverence that the summit of Maunakea has always had within the Native Hawaiian community. We are most fortunate to have the opportunity to conduct observations from this mountain.

C.C. and E.F.V. acknowledge the support of NASA Solar System Workings grant 19-SSW19-0190. C.C. acknowledges support from the Florida Space Grant Consortium. B.P. and F.L.R. acknowledge the support of the University of Central Florida Preeminent Postdoctoral Program (P³).

Appendix A Orbit Fitting

Observations from Keck followed the same procedures as past observations (e.g., W. M. Grundy et al. 2019b). As part of Keck program N193, we used the laser guide star adaptive optics system (P. L. Wizinowich et al. 2006) with the NIRC2 narrow camera.¹³ Images were taken with the *H* filter, with wavelengths between ~ 1.48 and $1.77 \mu\text{m}$. Relative astrometry was extracted from flat-fielded pairs of subtracted dithered images with Gaussian PSF fitting, using the same techniques as a variety of studies in the TNO binary literature (J. A. Stansberry et al. 2012; W. M. Grundy et al. 2019b). Observations from HST program 17848 were acquired with the Wide Field Camera 3 (WFC3) instrument using the F350LP filter. Our full astrometry dataset is shown in Table 3. Calibrated images from MAST had astrometry extracted using PSF fitting with model WFC3 PSFs from TinyTim using well-validated techniques (W. M. Grundy et al. 2019b). We implement a 2 mas noise floor on the astrometry to account for any systematic errors in the astrometric reduction (i.e., time-variable distortion of the NIRC2/WFC3 field, uncertainties in the distortion solution, uncertainties in pixel scale, etc.).

Orbit fitting was accomplished using MultiMoon, an orbit fitting software designed to fit the relative astrometry of TNO binaries (D. Ragozzine et al. 2024). MultiMoon is built on a Bayesian framework, approaching the orbit fitting problem as a task for Bayesian inference by using the emcee Markov Chain Monte Carlo sampler (D. Foreman-Mackey et al. 2013). We use the Keplerian orbit fitting module to fit Salacia–Actaea's mutual orbit. Although recent studies have found that Actaea's orbit may be better fit by a precessing non-Keplerian orbit (B. C. Proudfoot et al. 2024), the approximation of a Keplerian orbit still provides an extremely sensitive way to measure the mutual orbit period, system mass, and orbit orientation. We revisit the putative non-Keplerian nature of Actaea's orbit later.

Orbit fits were run using standard MultiMoon fitting procedures. We used an ensemble of 960 walkers that were run for 15,000 burn-in steps split between 10,000 initial steps and 5000 postpruning burn-in steps. The posterior distribution was then sampled using 10,000 steps, producing converged fits. For more specific details on the MultiMoon procedures and methods, see B. C. Proudfoot et al. (2024) and D. Ragozzine et al. (2024).

The results of our Keplerian orbit fits are shown in Table 1. Our fits achieve a best-fit $\chi^2 = 51.8$ with 26 degrees of freedom, giving a χ^2 per degree of freedom of 2.0, indicating a somewhat poor fit quality. We calculate the probability that random chance could give an equivalent (or worse) fit quality as 0.2%. A two-dimensional view of the orbit fitting residuals is shown in Figure 5. However, even with such a poor fit quality, typical residuals in astrometry are of order ~ 10 mas, showing that the Keplerian orbit provides an excellent approximation of Actaea's orbital motion. In our fits, we provide a new estimate of Actaea's orbit period, with uncertainties of ~ 1 s.

Our fits show that Actaea's prograde orbit seems to be eccentric, detecting a nonzero eccentricity at $\sim 2.5\sigma$ confidence. Given the system's tidally evolved state, this small undamped eccentricity is quite surprising, with estimates of the

¹³ <https://www2.keck.hawaii.edu/inst/nirc2>

Table 3
Observed Astrometric Positions of Actaea

Julian Date	Date	Telescope/Camera	Δx (arcsec)	Δy (arcsec)	$\sigma_{\Delta x}$ (arcsec)	$\sigma_{\Delta y}$ (arcsec)
2453938.41493	2006/07/21	HST/ACS-HRC	+0.04706	−0.10224	0.00200	0.00200
2454295.37924	2007/07/13	HST/WFPC2-PC	+0.02193	−0.11084	0.00391	0.01344
2454297.32976	2007/07/15	HST/WFPC2-PC	+0.12371	+0.09208	0.00448	0.00206
2454323.96413	2007/08/11	HST/WFPC2-PC	+0.17781	+0.00363	0.00200	0.00303
2454324.77860	2007/08/12	HST/WFPC2-PC	+0.12785	+0.09402	0.00391	0.00200
2454324.90898	2007/08/12	HST/WFPC2-PC	+0.10084	+0.09889	0.00863	0.00316
2454346.90493	2007/09/03	HST/WFPC2-PC	+0.10314	+0.09949	0.00358	0.00347
2454606.27369	2008/05/19	HST/WFPC2-PC	−0.10096	+0.07422	0.00200	0.00200
2455176.77133	2009/12/11	Keck II/NIRC2	+0.05801	+0.10558	0.00613	0.00300
2455411.90558	2010/08/03	Keck II/NIRC2	+0.18274	+0.01839	0.00300	0.00300
2456492.02668	2013/07/18	Gemini/NIRI	−0.19689	−0.07799	0.10000	0.10000
2456529.01220	2013/08/24	Gemini/NIRI	−0.06779	+0.11576	0.10000	0.10000
2457234.99390	2015/07/31	Keck II/NIRC2	+0.05868	−0.08215	0.00312	0.00654
2457606.96819	2016/08/06	Keck II/NIRC2	−0.18064	−0.05189	0.00300	0.00300
2459453.88191	2021/08/27	Keck/NIRC2	−0.07667	−0.12512	0.00223	0.00200
2460521.40133	2024/07/29	HST/WFC3	+0.16572	+0.01519	0.00200	0.00200
2460524.23293	2024/08/01	HST/WFC3	−0.16554	−0.03485	0.00200	0.00224

Notes. x and y correspond to R.A. and decl., respectively. Uncertainties on Δx , y have noise floors of 2 mas.

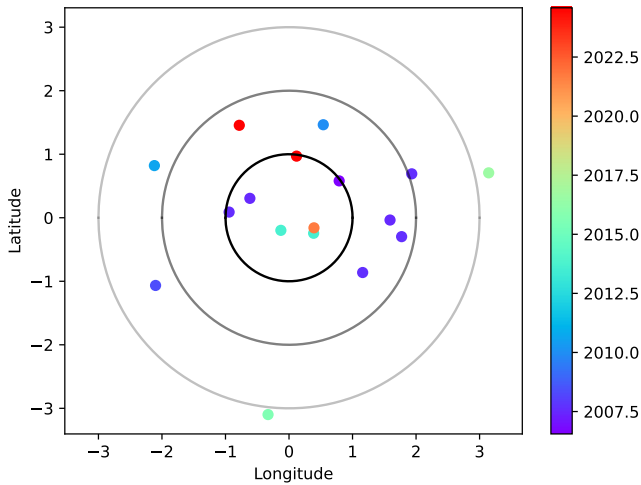


Figure 5. Two-dimensional view of the orbit fitting residuals. The color bar indicates the date of observation.

eccentricity damping timescale of <20 Myr (J. A. Stansberry et al. 2012). Two plausible scenarios could explain this: first, a recent perturbation—from an impact or a TNO flyby—could have excited the mutual orbit’s eccentricity, which has yet to be fully damped. Alternatively, small time-variable offsets between Salacia’s (or Actaea’s) center of body and center of light (COB-COL) could masquerade as a small orbital eccentricity. A similar residual eccentricity plagued Pluto–Charon orbit fits for decades, until accurate albedo maps of Pluto’s and Charon’s surfaces were convolved with precise HST astrometry (D. J. Tholen & M. W. Buie 1997; M. W. Buie et al. 2012). Given the system’s single-peaked lightcurve, which appears to be the result of rotating albedo features (see below), this explanation seems a plausible—and, importantly, parsimonious—explanation for the residual eccentricity detected in our orbit fits.

With our measured eccentricity, we can estimate the size of these COB-COL offsets, assuming that these offsets are

responsible for the entire eccentricity. The radial difference between apoapse and periapse is given as $\Delta r = 2ae \approx 91$ km. The required COB-COL offset would be a periodic function (phased to the mutual orbital motion) with an amplitude of $\Delta r/2 \approx 45$ km, or $\sim 5\%$ of Salacia’s diameter. In comparison, Pluto’s average COB-COL offset is $\sim 10\%$ of its diameter (M. W. Buie et al. 2010).

COB-COL variations may also be responsible for the poor fit quality found with a Keplerian orbit fit. Past works have suggested that the poor fit quality was due to non-Keplerian precession (B. C. Proudfoot et al. 2024). Importantly, however, in a tidally evolved system, non-Keplerian effects are generally minimized. Since the mutual orbital motion of Salacia and Actaea contain the majority of the system’s angular momentum, misalignments between Salacia’s rotation pole and the mutual orbit pole will tend to induce precession/libration of Salacia’s pole, effectively eliminating nodal precession. Since eccentricity is quickly damped (as discussed above), apsidal precession is also minimized. In contrast, COB-COL offsets, which move in phase with the system’s mutual orbital motion, can appear as a small, precessing eccentricity.

Appendix B Photometry Calibration

We utilized the Moose M2 (R. Morales et al. 2022) software to process FITS images from each observing run and output the photometry of the Salacia–Actaea system. The output photometry is in the Johnson–Cousins R band calibrated to the A. U. Landolt (1992) photometric system.

Photometric calibrations in M2 are done on an image-by-image basis as follows. M2 makes use of in-frame stars with known apparent magnitudes in the Gaia Early Data Release 3 catalog, along with the Gaia \rightarrow Johnson V - and Johnson R -band filter transformation equations published in M. Riello et al. (2021). The majority of our observations were done through no filter at all, so transformation equations had to be computed between the filter/camera response and the

A. U. Landolt (1992) photometric system. Filter transformation equations are a function of some stellar (and TNO) color index, and since most large TNOs have precise $V - R$ colors, M2 uses filter transformation equations that are measured using the $V - R$ color for main-sequence-type stars.

For each in-frame star within the Gaia catalog, the V - and R -band magnitudes are computed using the known filter transformation equations from M. Riello et al. (2021), along with the $V - R$ color. We refer to the R -band catalog magnitudes as R_{cat} . Instrumental fluxes are then measured for each star using basic aperture photometry, with source aperture and background annulus radii related to the measured stellar FWHM ($1.3 \times \text{FWHM}$ radius for the source aperture). For an instrumental magnitude of $m_{\text{in}} = -2.5 \log(F)$, the instrumental magnitude and R_{cat} are related by $R_{\text{cat}} - m_{\text{in}} = -Z + f(V - R)$, where Z is the zero-point and $f(V - R)$ is a third-order polynomial as a function of $V - R$ with coefficients B_1 , B_2 , and B_3 . The polynomial coefficients and zero-point are fitted with in-frame stars. For the TNO with flux F_{TNO} and known color $(V - R)_{\text{TNO}}$, the R -band magnitude on the A. U. Landolt (1992) system is

$$R_{\text{TNO}} = -2.5 \log(F) + Z + B_1(V - R) + B_2(V - R)^2 + B_3(V - R)^3|_{\text{TNO}}. \quad (\text{B1})$$

M2 has various stages that filter out poor images and poor calibration stars and ensures minimal contamination in the TNO flux. After M2 tabulated the photometry, we used additional filters and checks to ensure accurate photometry of the Salacia–Actaea system. We required there to be ≥ 10 calibration stars in each image. The color coefficients in the filter transformation equations for a given filter/camera combination should be constant in nature from night to night and image to image. As such, we tabulated the photometry for each filter/camera combination and ran a sigma-clipping routine for each of the color coefficients (at 3σ), filtering out observations where the color coefficients were extremal. Lastly, we ensured that the apertures used for the photometry were centered on the expected location of the TNO and that they tracked the TNO’s expected position over the course of each observing run and did not jump to nearby sources.

Appendix C Tidal Evolution Model

Assuming that Salacia’s spin pole is parallel to the orbit pole and that angular momentum is conserved, Salacia’s rotation period and the primaricentric semimajor axis evolve according to (P. Goldreich & S. Soter 1966; C. D. Murray & S. F. Dermott 1999)

$$\frac{d\Omega}{dt} = \text{sign}(n - \Omega) \frac{45G}{8} \left(\frac{R_p^3 m_s^2}{M_p} \frac{1}{Q'} \right) \left(\frac{1}{a^6} \right), \quad (\text{C1})$$

$$\frac{da}{dt} = -\text{sign}(n - \Omega) \frac{9\sqrt{G}}{2} \left(\frac{R_p^5 m}{\sqrt{M}} \frac{1}{Q'} \right) \left(\frac{1}{a^{11/2}} \right), \quad (\text{C2})$$

where Ω is Salacia’s spin angular velocity, n is the mean motion, G is the gravitational constant, R_p is the radius of Salacia, M_p is the mass of Salacia, m_s is the mass of Actaea, a

is the primaricentric semimajor axis, and












$$Q' = Q \left(1 + \frac{57}{8\pi G} \frac{\mu}{R_p^2 \rho_p^2} \right) \quad (\text{C3})$$

for a dimensionless tidal dissipation factor Q , modulus of rigidity μ , and mass density ρ . Salacia’s and Actaea’s diameters are $D_p = 866 \pm 37$ km and $D_s = 290 \pm 21$ km, respectively (M. E. Brown & B. J. Butler 2017). The total mass is $M_{\text{sys}} = (486.1 \pm 7.5) \times 10^{18}$ kg (Table 1).

For the modulus of rigidity, we used $\mu = 4$ GPa, which is representative of water ice (J. J. Neumeier 2018). Although a rigidity of $\mu \simeq 67$ GPa (typical of solid rock) has been used in the past, Salacia’s bulk material properties during the initial ~ 1000 Myr when tidal evolution occurred is not well modeled as a solid monolith. We note that if Salacia differentiated sufficiently fast (within ~ 100 Myr) and hosts a large monolithic rocky core, this would decrease the dissipation in the interior, increasing the tidal evolution timescales. Indeed, Salacia today may be differentiated with a rocky core; however, this required an epoch of melting, where water percolated through the pores of a rocky matrix before refreezing (S. Loveless et al. 2022).

In this work, the evolution of the Salacia–Actaea system was evaluated numerically using Equations (C1) and (C2) and Euler’s method. This numerical method has several benefits, including (a) allowing multiple changes in the sign ($n - \Omega$) argument during evolution and (b) conservation of the physical parameters that control the migration timescale.

ORCID iDs

Cameron Collyer  <https://orcid.org/0009-0004-7149-5212>
Estela Fernández-Valenzuela  <https://orcid.org/0000-0003-2132-7769>
Jose Luis Ortiz  <https://orcid.org/0000-0002-8690-2413>
Bryan J. Holler  <https://orcid.org/0000-0002-6117-0164>
Benjamin Proudfoot  <https://orcid.org/0000-0002-1788-870X>
Nicolás Morales  <https://orcid.org/0000-0003-0419-1599>
Rafael Morales  <https://orcid.org/0000-0003-1661-0594>
Susan Benecchi  <https://orcid.org/0000-0001-8821-5927>
Flavia L. Rommel  <https://orcid.org/0000-0002-6085-3182>
Will Grundy  <https://orcid.org/0000-0002-8296-6540>
Darin Ragozzine  <https://orcid.org/0000-0003-1080-9770>

References

- Akiba, R., & Nimmo, F. 2025, Thermal–Orbital Evolution of Eris, *Icar*, **443**, 116770
- Alexandersen, M., Benecchi, S. D., Chen, Y.-T., et al. 2019, OSSOS. XII. Variability Studies of 65 Trans-Neptunian Objects Using the Hyper Suprime-Cam, *ApJS*, **244**, 19
- Arakawa, S., Hyodo, R., & Genda, H. 2019, Early Formation of Moons Around Large Trans-Neptunian Objects via Giant Impacts, *NatAs*, **3**, 802
- Arakawa, S., Hyodo, R., Shoji, D., & Genda, H. 2021, Tidal Evolution of the Eccentric Moon Around Dwarf Planet (225088) Gonggong, *AJ*, **162**, 226
- Arakawa, S., Kamata, S., & Genda, H. 2025, Low Rock Mass Fraction within Trans-Neptunian Objects Inferred from the Spin–Orbit Evolution of Orcus–Vanth and Salacia–Actaea, *JGRE*, **130**, e2024JE008923
- Ashton, E., Chang, C.-K., Chen, Y.-T., et al. 2023, FOSSIL. III. Lightcurves of 371 Trans-Neptunian Objects, *ApJS*, **267**, 33
- Astropy Collaboration, Price-Whelan, A. M., Lim, P. L., et al. 2022, The Astropy Project: Sustaining and Growing a Community-oriented Open-source Project and the Latest Major Release (v5.0) of the Core Package, *ApJ*, **935**, 167

- Astropy Collaboration, Price-Whelan, A. M., Sipőcz, B. M., et al. 2018, The Astropy Project: Building an Open-science Project and Status of the v2.0 Core Package, *AJ*, **156**, 123
- Astropy Collaboration, Robitaille, T. P., Tollerud, E. J., et al. 2013, Astropy: A Community Python Package for Astronomy, *A&A*, **558**, A33
- Benecchi, S. D., Noll, K. S., Grundy, W. M., et al. 2009, The Correlated Colors of Transneptunian Binaries, *Icar*, **200**, 292
- Bernstein, G. M., Holler, B. J., Navarro-Escamilla, R., et al. 2023, Synchronous Rotation in the (136199) Eris-Dysnomia System, *PSJ*, **4**, 115
- Bierson, C. J., & Nimmo, F. 2019, Using the Density of Kuiper Belt Objects to Constrain their Composition and Formation History, *Icar*, **326**, 10
- Brown, M. E. 2012, The Compositions of Kuiper Belt Objects, *AREPS*, **40**, 467
- Brown, M. E., & Butler, B. J. 2017, The Density of Mid-sized Kuiper Belt Objects from ALMA Thermal Observations, *AJ*, **154**, 19
- Brown, M. E., & Butler, B. J. 2023, Masses and Densities of Dwarf Planet Satellites Measured with ALMA, *PSJ*, **4**, 193
- Buie, M. W., Grundy, W. M., Young, E. F., Young, L. A., & Stern, S. A. 2010, Pluto and Charon with the Hubble Space Telescope. II. Resolving Changes on Pluto's Surface and a Map for Charon, *AJ*, **139**, 1128
- Buie, M. W., Tholen, D. J., & Grundy, W. M. 2012, The Orbit of Charon is Circular, *AJ*, **144**, 15
- Christy, J. W., & Harrington, R. S. 1978, The Satellite of Pluto, *AJ*, **83**, 1005
- Foreman-Mackey, D., Conley, A., Meierjürgen Farr, W., et al., 2013 emcee: the MCMC Hammer, Astrophysics Source Code Library, ascl:1303.002
- Fornasier, S., Lellouch, E., Müller, T., et al. 2013, TNOs are Cool: A Survey of the Trans-Neptunian Region, *A&A*, **555**, A15
- Fraser, W. C., Pike, R. E., Marsset, M., et al. 2023, Col-OSSOS: The Two Types of Kuiper Belt Surfaces, *PSJ*, **4**, 80
- Ginsburg, A., Sipőcz, B.M., Marsset, M., et al. 2019, Astroquery: An Astronomical Web-querying Package in Python, *AJ*, **157**, 98
- Gladman, B., & Volk, K. 2021, Transneptunian Space, *ARA&A*, **59**, 203
- Goldreich, P., & Soter, S. 1966, Q in the Solar System, *Icar*, **5**, 375
- Grundy, W. M., Noll, K. S., Buie, M. W., et al. 2019a, The Mutual Orbit, Mass, and Density of Transneptunian Binary G!kún||'hòmdímà (229762 2007 UK126), *Icar*, **334**, 30
- Grundy, W. M., Noll, K. S., Roe, H. G., et al. 2019b, Mutual Orbit Orientations of Transneptunian Binaries, *Icar*, **334**, 62
- Holler, B. J., Grundy, W. M., Buie, M. W., & Noll, K. S. 2021, The Eris/Dysnomia System I: The Orbit of Dysnomia, *Icar*, **355**, 114130
- Kiss, C., Pál, A., Szakáts, R., Marton, G., & Müller, T. 2020, *EPSC*, **14**, EPSC2020-516
- Lacerda, P., Fornasier, S., Lellouch, E., et al. 2014, The Albedo-Color Diversity of Transneptunian Objects, *ApJL*, **793**, L2
- Landolt, A. U. 1992, UBVR Photometric Standard Stars in the Magnitude Range 11.5, *AJ*, **104**, 340
- Lomb, N. R. 1976, Least-squares Frequency Analysis of Unequally Spaced Data, *Ap&SS*, **39**, 447
- Loveless, S., Privalnik, D., & Podolak, M. 2022, On the Structure and Long-term Evolution of Ice-rich Bodies, *ApJ*, **927**, 178
- McMaster, M., Turner, A. M., Antonov, I. O., et al. 2008, Wide Field and Planetary Camera 2 Instrument Handbook v10.0 (Baltimore, MD: STScI)
- Morales, R., Morales, N., Duffard, R., et al. 2022, *EPSC*, **16**, EPSC2022-652
- Murray, C. D., & Dermott, S. F. 1999, Solar System Dynamics (Cambridge: Cambridge Univ. Press), 130
- Neumeier, J. J. 2018, Elastic Constants, Bulk Modulus, and Compressibility of H₂O Ice Ih for the Temperature Range 50 K-273 K, *JPCRD*, **47**, 033101
- Nimmo, F., & Brown, M. E. 2023, The Internal Structure of Eris Inferred from its Spin and Orbit Evolution, *SciA*, **9**, eadi9201
- Proudford, B. C., Ragozzine, D. A., Thatcher, M. L., et al. 2024, Beyond Point Masses. II. Non-Keplerian Shape Effects Are Detectable in Several TNO Binaries, *AJ*, **167**, 144
- Ragozzine, D., Pincock, S., Proudford, B. C., et al. 2024, Beyond Point Masses. I. New Non-Keplerian Modeling Tools Applied to Trans-Neptunian Triple (47171) Lempo arXiv:2403.12785
- Riello, M., De Angeli, F., Evans, D. W., et al. 2021, Gaia Early Data Release 3. Photometric Content and Validation, *A&A*, **649**, A3
- Scargle, J. D. 1982, Studies in Astronomical Time Series Analysis. II. Statistical Aspects of Spectral Analysis of Unevenly Spaced Data, *ApJ*, **263**, 835
- Stansberry, J. A., Grundy, W. M., Mueller, M., et al. 2012, Physical Properties of Trans-Neptunian Binaries (120347) Salacia-Actaea and (42355) Typhon-Echidna, *Icar*, **219**, 676
- Szakáts, R., Kiss, C., Ortiz, J. L., et al. 2023, Tidally Locked Rotation of the Dwarf Planet (136199) Eris Discovered via Long-term Ground-based and Space Photometry, *A&A*, **669**, L3
- Thirouin, A., Noll, K. S., Ortiz, J. L., & Morales, N. 2014, Rotational Properties of the Binary and Non-binary Populations in the trans-Neptunian Belt, *A&A*, **569**, A3
- Tholen, D. J., & Buie, M. W. 1997, The Orbit of Charon, *Icar*, **125**, 245
- VanderPlas, J. T. 2018, Understanding the Lomb-Scargle Periodogram, *ApJS*, **236**, 16
- Verbitser, A. J., Helfenstein, P., Porter, S. B., et al. 2022, The Diverse Shapes of Dwarf Planet and Large KBO Phase Curves Observed from New Horizons, *PSJ*, **3**, 95
- Vilenius, E., Kiss, C., Mommert, M., et al. 2012, "TNOs are Cool": A Survey of the Trans-Neptunian Region. VI. Herschel/PACS Observations and Thermal Modeling of 19 Classical Kuiper Belt Objects, *A&A*, **541**, A94
- Wizinowich, P. L., Le Mignant, D., Bouchez, A. H., et al. 2006, The W. M. Keck Observatory Laser Guide Star Adaptive Optics System: Overview, *PASP*, **118**, 297